Additive Manufacturing 121 (2026) 105149

Contents lists available at ScienceDirect

Additive Manufacturing

journal homepage: www.elsevier.com/locate/addma

Research paper

Dynamics of material redistribution and microstructure formation in Al–Cu multimaterial

Steve Gaudez [a,*], Andaç Özsoy [a], Yunhui Chen [b], William Hearn [a], Alexander Rack [c], Steven Van Petegem [a,*]

[a] Laboratory for Condensed Matter, PSI Center for Photon Science, Forschungsstrasse 111, 5232 Villigen PSI, Switzerland
[b] School of Engineering, RMIT University, Melbourne, Australia
[c] ESRF – The European Synchrotron, Structure of Materials Group - ID19, F-38043, Grenoble Cedex 9, France

ARTICLE INFO

Keywords:
Additive manufacturing
Functionally graded materials
Fluid flows
Operando
X-ray imaging

ABSTRACT

Additive manufacturing (AM) enables the precise fabrication of multimaterial components; however, Achieving chemical and structural homogeneity at material interfaces remains a significant challenge. Existing research on material transport in AM primarily relies on numerical simulations and postmortem analyses, with real-time, three-dimensional characterization still lacking. In this study, we employ in situ X-ray radiography and X-ray computed tomography to investigate material redistribution during laser powder bed fusion of a Al–CuCrZr multimaterial. Our results demonstrate that the incorporation of Cu occurs through discrete, stochastic events within the melt pool. We suggest that this mode of incorporation results from the poor wetting of the spreading liquid on the substrate liquid, necessitating additional dynamic driving forces to assist the incorporation process. Within the melt pool, copper mixing is predominantly governed by fluid dynamics, with relatively negligible effects from gravitational/buoyancy and viscous forces, as well as diffusion. However, despite the high fluid velocity, heterogeneous local compositions persist. These variation of local composition, in turn, lead to shifts in the local solidification path and ultimately influence the resulting microstructure. The predominant mixing mechanisms and length scales are likely applicable to a wider range of multimaterial systems. Additionally, the incorporation mode could be expected to hold for multimaterial systems sharing similar wetting behavior, but requires further investigations for confirmation. These findings offer valuable experimental validation for numerical models and provide key insights to guide the optimization of future multimaterial AM processes.

1. Introduction

Laser powder bed fusion (LPBF) is an additive manufacturing (AM) technology that enables the fabrication of complex, near-net-shaped three-dimensional metallic components through a layer-by-layer melting process [1]. The ability to process a wide range of metals, including aluminum (Al), titanium (Ti), copper (Cu), and iron (Fe), has expanded its applications across industries such as aerospace, biomedical, and energy [2–5]. A major advantage of LPBF is the precise local control over processing parameters, allowing for tailored microstructures and compositional gradients within a single part. This capability has led to the development of functionally graded materials (FGMs) [6], heterostructured alloys [7], and stimulus-responsive [8,9], also referred as 4D printing, microstructures with enhanced mechanical, thermal, and electrical properties.

Beyond microstructural control, multimaterial processing in AM processes has opened new opportunities for integrating materials with distinct properties to create advanced engineering structures. By selectively depositing different materials, composition can be varied either abruptly, by printing one material on top of or adjacent to another, or gradually through the spatial control of the composition of the printed material enabled via the premixing of different feedstock materials [6,10,11]. This design freedom facilitates the development of complex engineering structures [12], that exploit the advantageous physical, chemical, and mechanical properties of their constituent materials, such as electrical and thermal conductivity, corrosion resistance, and enhanced mechanical performance. By combining these distinct characteristics, the resulting multimaterial exhibits novel physicochemical properties not found in its individual components. Additionally, in situ alloying provides opportunities for rapid prototyping

* Corresponding authors.
E-mail addresses: steve.gaudez@psi.ch (S. Gaudez), steven.vanpetegem@psi.ch (S. Van Petegem).

https://doi.org/10.1016/j.addma.2026.105149
Received 20 November 2025; Received in revised form 2 March 2026; Accepted 2 March 2026
Available online 4 March 2026

of innovative alloys [13]. Due to their exceptional design flexibility, AM processes offer considerable potential for producing sustainable and cost-effective multimaterial solutions through precise local control over microstructure and composition that are hardly achievable by conventional manufacturing processes.

Despite the potential of multimaterial AM, fabricating defect-free components remains a significant challenge. Material heterogeneities during multimaterial LPBF can lead to chemical segregation, the formation of brittle intermetallic phases, residual stresses, cracking, and porosity [6,11,14,15]. These issues arise due to differences in material properties, including melting temperature, thermal expansion coefficients, and chemical affinities, as well as variations in optimal processing parameters such as laser power and scan speed. Achieving composition homogeneity at the melt pool scale is particularly challenging, as rapid solidification limits the time available for diffusion and mixing [11,14,16–18]. This results in localized variations in phase formation, grain structure, and mechanical properties, ultimately impacting part performance.

Various approaches have been explored to mitigate these challenges, including remelting strategies [19] and post-processing heat treatments [17] to promote better material homogenization. However, these techniques add complexity, are energy-intensive, and could introduce unwanted microstructural changes, such as recovery, phase transformation, and recrystallization. Furthermore, defects such as cracks or voids can remain embedded within the material despite these additional steps. Additionally, high energy density has been shown to promote remelting and remixing of the underlying layers during multimaterial printing, leading to increased homogeneity and a wider interfacial region [20]. Another approach to mitigate these challenges is by adding an interlayer of a third material at the interface, which will accommodate the difference in thermal and physical properties of the two initial compound of the multimaterial and prevent the formation of brittle phases. This approach was successfully applied for example to Ti–Al [21] and Cu–W [22] multimaterial combinations with Cu and stainless steel interlayers, respectively. While this strategy can effectively suppress the formation of brittle phases, it does not necessarily prevent the formation of undesired phases or defects, e.g., intermetallic and cracks [22]. Additionally, the mechanical bottleneck may shift to the intrinsic properties of the interlayer and to the quality of the bounds with the base materials. Similarly to remelting strategy and post-processing treatments, the use of a third material add process complexity. Finally, the multimaterial printing sequence appears to be a critical parameter, as it can enhance mixing and prevent defect formation [23,24]. For example, the higher heat dissipation of Cu alloy when used as substrate to print a Ni alloy leads to a shorter melt pool lifetime, contrarily to the reverse, and ultimately to a higher degree of chemical heterogeneity [24].

Chemical heterogeneities primarily arise from the rapid solidification characteristic of LPBF, which significantly limits the time spent in the liquid phase and thereby restricts solute mass transport, as shown in [25]. These heterogeneities influence local solidification paths, resulting in variations in grain size, crystallographic texture, microstructure, phase nature, and phase fractions in the solidified material [11,26–29]. Consequently, these microstructural variations can lead to defects and undesirable material properties. Nevertheless, controlled chemical heterogeneities can be strategically beneficial for manipulating phase stability and enhancing mechanical properties [16,30]. Therefore, to fully leverage the design potential of multimaterial additive manufacturing processes, a thorough understanding of the underlying mechanisms of solute mass transport within the melt pool is critical. However, most research has focused on optimizing multimaterial processability rather than elucidating the underlying mechanisms.

Understanding mass transport and mixing in LPBF is inherently complex due to the wide range of processing conditions (e.g., conduction vs. keyhole mode melting), differences in material properties (e.g., melting point, and viscosity), and rapid phase transformations. Moreover, this complexity is further heightened by the fact that only a handful of advanced techniques are capable of such real-time characterization. To overcome these limitations, numerical models have been widely used to simulate material transport, keyhole formation, and pore evolution, providing valuable insight into how processing parameters affect the final microstructure [31–37]. Additionally, high-fidelity simulations have been employed to study segregation, evaporation, and redistribution phenomena in AM melt pools [38,39] as well as the effect of turbulences in the fluid flow [40]. However, these models are typically validated using post mortem one- or two-dimensional chemical analyses, which fail to capture the real-time, three-dimensional dynamics of melt pool behavior. As a result, current models struggle to accurately predict phase formation and final microstructures in multimaterial systems where phase evolution is highly sensitive to localized composition changes. The lack of real-time experimental data significantly limits the ability to compare and refine numerical models, making it difficult to optimize multimaterial AM processes effectively. Recently, studies have opened the way of such characterization with the investigation of an in situ alloyed Al–50 vol%Sn powder [14] and AlSi7Mg–CuCrZr powder [41], and 316L or In718 powder on Al alloy substrates [42] during single-track LPBF, focusing on fluid flow and keyhole instabilities and crack formation. Addressing this lack of studies is critical for advancing multimaterial AM and improving predictive modeling capabilities.

To overcome these limitations, this work presents a real-time experimental investigation into material transport and chemical evolution within the melt pool during multimaterial LPBF. Using in situ high-speed X-ray imaging (100,000 images s^{-1}) with micrometer-scale resolution, we capture the redistribution of material in an Al–Cu system during processing. The Al–Cu system was chosen due to its technological importance and strong relevance in high performance applications where optimizing mechanical, thermal, and electrical properties is essential, such as in the sectors of energy and transportation [17,18,34,43–46]. Additionally, methodological consideration played a significant role in this choice. Image-based experiments at synchrotron or free electron beamlines are the only method capable of providing the dynamics of the composition in the melt pool with a good temporal and spatial resolutions. Due to the constrains related to the experimental setup and X-ray matter interactions (e.g., sample thickness and X-ray absorption), the Al–Cu system appears to be one of the best compromises for studying compositional changes in real-time using X-ray imaging techniques during fast processing. To do so, consecutive single tracks were printed under controlled conditions to study the effects of multiple-layer deposition. Additionally, post-process X-ray microtomography was used to analyze the final three-dimensional chemical distribution, complementing the real-time imaging results. The resulting microstructure was further characterized through a combination of X-ray diffraction and scanning electron microscopy complemented by energy-dispersive X-ray spectroscopy.

By combining real-time X-ray imaging, microtomography, and microstructural characterization, this study provides unprecedented insights into material mixing, melt pool dynamics, and solidification mechanisms in multimaterial LPBF. These findings serve as critical experimental validation for numerical models and offer a foundation for future work in optimizing processing strategies for multimaterial AM.

2. Material and methods

2.1. Material and printing parameters

The feedstock powder used in this study was a Cu–0.9Cr–0.07Zr alloy (in wt%) with trace amounts of Fe, Si, and O, supplied by m4p (Austria). The powder granulometry is d10 = 38 μm, d50 = 49 μm, and d90 = 61 μm. Four sequential single-track layers were printed onto a commercially pure Al (99.99%) base plate with dimensions of

12×10 mm^2 (x, z) and a thickness of 0.5 mm along the y-axis. The base plates were laser-cut from a 0.5 mm thick sheet; the specific edge where printing occurred was polished and cleaned prior to the experiments. The experiments were conducted in an Ar atmosphere using the MiniSLM machine [47] which is specifically designed for synchrotron-based operando studies. To facilitate transmission-mode X-ray imaging, the setup was tilted by 4° around the x axis. The printing parameters were as follows: laser power of 200 W, scanning speed of 500 mm s^{-1}, layer height of ~50 μm, a focused laser beam diameter ($1/e^2$) of 33 μm, and unidirectional printing strategy. These parameters were chosen to study the dynamics of the melt pool under industrially relevant conditions, i.e., scanning speed, while ensuring effective melting of copper-based powder and allowing the study of mass transport, keyhole, and bubble/pore evolution through the keyhole regime. The scanning speed also results from a compromise between temporal and spatial resolutions and field-of-view during the X-ray imaging experiments.

2.2. X-ray imaging experiments

X-ray imaging experiments were conducted at the ID19 beamline of the European Synchrotron Radiation Facility (ESRF, France) using the MiniSLM system [47]. The beamline was configured in white-beam mode, with a single-harmonic undulator source (U17.6) and gaps set to 11.8 mm for operando radiography and 25.7 mm for microtomography. A diamond and beryllium window were the mandatory X-ray optical elements in the X-ray beam path (peak energy at 19 keV). For fast radiography, two compound-refractive lenses (beryllium) were inserted into the beam path to increase photon flux density on the detector. Two types of X-ray imaging experiments were performed:

2.2.1. Operando X-ray radiography

Operando radiography was conducted using a CMOS-based camera (Photron SAZ, Japan), coupled with a 250 μm-thick LuAg:Ce single-crystal scintillator and a 5× lens (0.14 numerical aperture, Mitutoyo, Japan). The optical system enabled a high-speed acquisition rate of 100,000 images s^{-1} with a 4.14 μm pixel size and a 2.8×1 mm^2 (x, z) field of view. Flat-field correction was applied to all images to compensate for variations in beam intensity.

Fig. 1 illustrates the experimental setup and workflow used for conducting and analyzing the operando experiments. To enable imaging, a thin powder bed was confined between two glassy carbon windows (Fig. 1b). The process was captured in real-time, with four sequential single tracks recorded during AM (see Supplementary Videos 1–4). Representative images from the first track are shown in Fig. 1c. A distinct contrast is observed between the Cu powder and the Al base plate, attributed to their respective effective densities and X-ray mass attenuation coefficients. The interaction between these two materials is also visible, highlighting the redistribution of Cu within the melt pool. Additionally, keyhole and pore structures appear as bright regions due to their lower X-ray attenuation (which results from the reduced mean density in the projected plane compared to Al) enhanced as well by refraction effects which highlight interfaces. Using known material properties and the experimental setup, the local composition was retrieved from X-ray mass attenuation data, as shown in Fig. 1c. A region of interest, marked by a red dashed rectangle in the raw images, was selected for further quantitative analysis.

2.2.2. X-ray microtomography

Microtomography experiments were performed using a CMOS-based camera (pco.edge 5.5, PCO AG, Germany), coupled with a 10 μm-thick GGG:Eu single-crystal scintillator and a 10× lens (0.3 numerical aperture, Olympus, Japan), resulting in a voxel size of $0.6 \times 0.6 \times 0.6$ μm^3. Tomographic reconstructions were processed using the Tomwer software (v1.3.13) with flat-field correction and normalization. No phase retrieval filter was applied to preserve X-ray mass attenuation measurements of the materials. For the X-ray microtomography experiments, four additional samples were manufactured with one to four layer addition to characterize independently each set of layer addition.

2.3. X-ray imaging analysis

2.3.1. Cu concentration mapping

Cu concentration maps were derived by converting pixel and voxel intensities to mass fraction values using the Beer–Lambert law and mixture/compound laws [48]. The contribution of Cr and Zr was neglected due to their low concentrations. Following previous studies [49] the X-ray mass attenuation coefficients were assumed at 19 keV with $(\mu/\rho)_{\mathrm{Cu,19\ keV}} = 38.90$ cm^2 g^{-1} and $(\mu/\rho)_{\mathrm{Al,19\ keV}} = 3.99$ cm^2 g^{-1}. These values were calculated using the XrayDB Python package (v4.5.3). Room-temperature densities of solid Cu (8.96 g cm^{-3}) and Al (2.7 g cm^{-3}) were used, resulting in a maximum estimation error below 0.02 wt Cu in the liquid state.

2.3.2. Data processing and visualization

Further data analysis, material segmentation, and visualization were performed using: ImageJ (2.14.0/1.54f), Python (3.10.12), and Dragonfly (2024.1).

2.4. Microstructural characterization

2.4.1. X-ray diffraction analysis

As-built X-ray diffraction (XRD) measurements were conducted at the P23 beamline of DESY-PETRA III (Hamburg, Germany) in transmission geometry. The setup consisted of a Pilatus 1M (Dectris, Switzerland) detector, a monochromatic beam $E = 20.5$ keV and a beam size of 200×20 μm^2 (x, z). Partial Debye–Scherrer rings were collected along a 2 mm horizontal scan (x-direction) to improve grain statistics. Data was radially integrated using the pyFAI Python library [50], with LaB_6 powder calibration to obtain detector position and tilt. Phase identification was performed using GSAS-II software (v5784) [51].

2.4.2. Scanning electron microscopy and energy-dispersive X-ray spectroscopy (EDX)

For scanning electron microscopy (SEM) characterization, the L3 sample was sectioned along the y–z plane. The cross-section was cut using an Ar-ion milling system (Hitachi IM4000) at 6 kV for 8 h with no tilt angle. A Zeiss ULTRA 55 SEM equipped with an EXTREME (Oxford) detector was used for SEM-EDX (energy-dispersive X-ray spectroscopy) analysis. Imaging and elemental mapping were performed at an accelerating voltage of 10 kV.

2.4.3. Phase diagram calculation

To support phase analysis, the Al–Cu phase diagram was calculated using Thermo-Calc (v2022b) with the TCAL8 (v8.1) aluminum database and the binary phase calculation module. Only Al and Cu were considered in these simulations.

3. Results and discussion

3.1. Real-time Cu distribution

Fig. 2a presents the projected Cu composition time series during the deposition of the fourth layer, focusing on the base plate (Cu powder is omitted for clarity). Keyhole, bubbles, and pores are highlighted in white, while black dotted lines indicate the estimated melt pool boundary. The keyhole formation results from the high energy density required to melt Cu powder. The Cu composition varies between 0 and 0.2 wt, a relatively low range due to the projection of Cu through the 0.5 mm-thick Al base plate and the limited width of the printed track (~0.25 mm).

The results reveal that Cu incorporation into Al occurs primarily through stochastic, discrete events, rather than a continuous flow into the melt pool. On a macroscopic scale, liquid Cu is initially drawn from the melt pool surface (Fig. 2a1–2) before sinking (Fig. 2a2–6) supporting the observations in [42]. Additionally, Cu is advected from

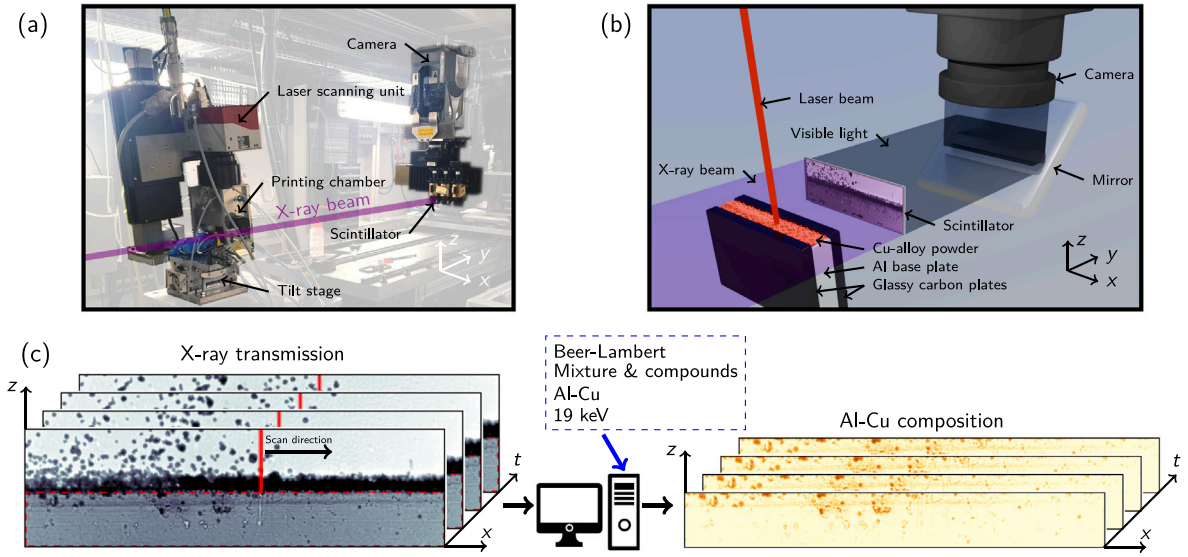

Fig. 1. Experimental setup and analysis method: (a) photography of the experimental setup at the ID19 ESRF beamline, (b) schematic illustration of the operando X-ray imaging during the LPBF processing of Cu alloy powder on Al base plate, and (c) example of raw images acquired during the process, showing the Cu alloy powder, Al base plate, and keyhole. The raw images are converted into Al–Cu composition images using the material and experimental setup characteristics. The red dashed rectangle indicates the region of interest used for data processing.

the trailing side of the melt pool and influenced by keyhole dynamics, where it can be either entrained or expelled (see Supplementary Videos 1–4). Over time, the Cu concentration within these occurrences diminishes. Furthermore, at later stages, Cu is displaced by the advancing solid/liquid interface (Fig. 2a7–8). The blue cross in Fig. 2a1–8 highlights the position, while the purple to blue line in Fig. 2a8 highlights the trajectory and velocity of the overall transport behavior.

The discrete Cu incorporation into Al indicates that specific conditions, such as wetting transition, Maragoni convection, or hydrodynamic fluctuations, must be met. Under static conditions, wetting is characterized by the spreading coefficient $S = \gamma_{sa} - \gamma_{la} - \gamma_{sl}$, where γ_{sa} is the surface tension of substrate liquid, γ_{sl} is the surface tension of spreading liquid, and γ_{la} the interfacial tension between the two liquids. Complete wetting occurs for $S > 0$, whereas for $S < 0$, partial or even no wetting if expected when $S \ll 0$. Since γ_{la} is generally difficult to determine, the inequality $0 < \gamma_{sa} - \gamma_{la} - \gamma_{sl}$ can be rearranged as $\gamma_{la} < \gamma_{sa} - \gamma_{sl}$. Given that $\gamma_{sl} > \gamma_{sa}$ for the Al–Cu system up to boiling temperatures (Table 1), the condition $S > 0$ would require $\gamma_{la} < 0$, which is thermodynamically impossible. Consequently, assuming pure Al and Cu, spontaneous wetting cannot occur. Additional driving forces — such Marangoni convection or local hydrodynamic fluctuations — must therefore assist the process, explaining the stochastic and discrete nature of the Cu incorporation into Al. Although some incorporation events coincide with keyhole collapse, this is not systematic, and minor contamination or oxide formation may further modify interfacial energies and the dominant incorporation mechanism.

Fig. 2b and c illustrate representative Cu motion trajectories and velocity profiles for each added layer (additional measurements are provided in Supplementary Figure 1). The trajectories presented in the present manuscript were manually tracked using ImageJ. Cu initially sinks into the melt pool while being displaced in the opposite direction of the laser scan. The velocity peaks as Cu enters the melt pool, then asymptotically decreases as the residence time in the liquid state increases, eventually stabilizing upon solidification. Maximum projected velocities reach approximately 1000 mm s^{-1} (see Supplementary Figure 1).

However, due to the 2D projection, the measured velocities represent a lower bound, as the transverse displacement (along the y-axis) is not accounted for. As a first reasonable hypothesis, the transverse displacement can be assumed to be of the same order of magnitude as the in-plane displacements, defined as $\Delta y = \max(\Delta x, \Delta z)$. Following this analysis, the difference between the 2D and 3D estimated velocities can be as high as 250 mm s^{-1} but decreases drastically over the melt pool lifetime. Consequently, the projected 2D velocities are considered sufficient for an order of magnitude analysis.

At finer scales, the mixing process exhibits complex fluid dynamics during these stochastic Cu occurrences. A Cu occurrence is defined as a discrete event in which a substantial volume of Cu is entrained and redistributed within the melt pool. Fig. 3 provides further insight, presenting (a) the univariate image differencing method employed to resolve small-scale transport phenomena, (b) a schematic of the methodology, and (c) a plot of time evolution and velocity variations. The univariate image differencing [52] is a method employed to identify changes between two images by subtracting the pixel values of one image from another, thereby accentuating the differences. In Fig. 3a1–3, Cu is drawn into the melt pool, subsequently breaking into smaller fragments (Fig. 3a4–7), contributing to material mixing at a microscale. Furthermore, Fig. 3c shows that near the keyhole position, the liquid metal exhibits upward and lateral flow, counteracting the primary Cu motion. These findings suggest that the introduction of a significant Cu volume into the melt pool induces a vortex-like flow pattern, driven by local hydrodynamic instabilities (Fig. 3c). As previously mentioned, liquid-phase velocity peaks at the onset of these occurrences before gradually decaying over time.

These observations contrast with the steady-state melt pool dynamics typically observed in monolithic material AM, where fluid flow is predominantly governed by inward or backward motion due to recoil pressure and the Marangoni effect [32,53,54]. In contrast, the presence of two distinct materials with significantly different physical properties may introduce additional complexity, as discussed in the following section. The maximum flow velocity $v = 1$ m s^{-1} is used in the following calculations; thus, the results should be considered as an upper bound regarding this variable.

The flow regime of the fluid is first characterized using the Reynolds number (Re):

$$Re = \frac{\rho v L}{\mu} \tag{1}$$

where ρ is the liquid density, v is the flow velocity, L is the melt pool length set at 500×10^{-6} m (see Fig. 2), and μ is the dynamic

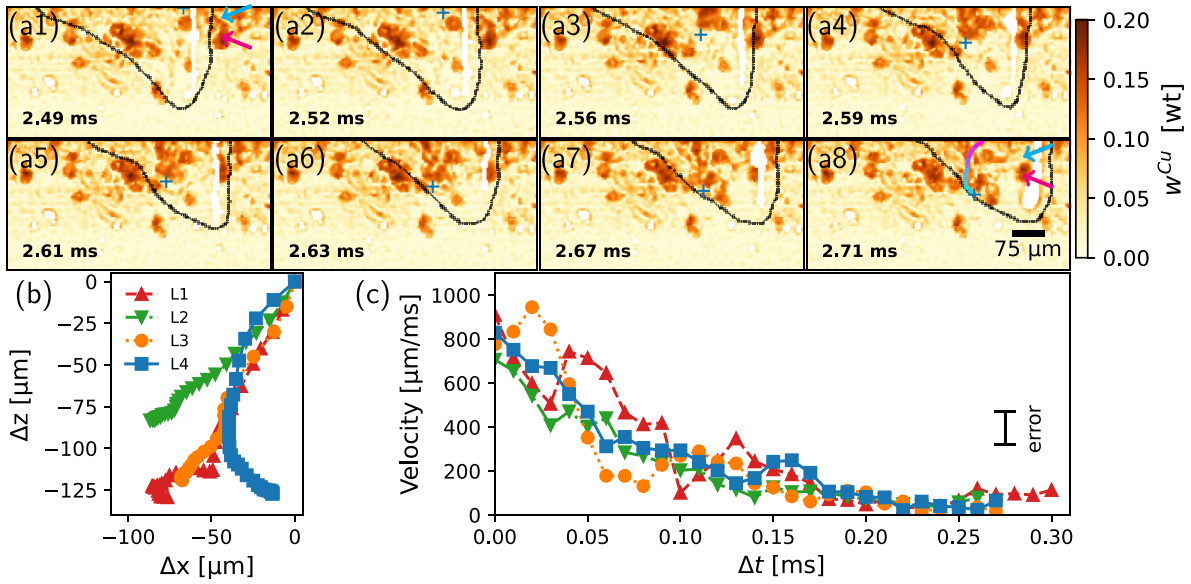

Fig. 2. Real-time Cu composition mapping and dynamic characterizations of an event during Al–Cu multimaterial AM. (a1–8) Snapshots of projected (x–z) Cu composition maps during the printing of L4, wherein an estimate of melt pool geometry (gray lines) and keyhole/pores (white areas) are overlaid. Projected relative motion trajectories (b), i.e, $\Delta x = x - x_0$ and $\Delta z = z - z_0$, and velocities (c), i.e, $\Delta t = t - t_0$, of Cu mixing discrete occurrences for L1–4 in the melt pool onto the x–z plane. Results in (b and c) for L4 stem for the blue crosses displayed in (a); the total motion path and its velocity (color scale) are overlaid in (a8). Blue and pink arrows in (a1) and (a8) indicate a remixing occurrence and a Cu powder particle stuck on the glassy carbon window, respectively.

viscosity of the liquid. Generally, for pipe geometry, laminar flow is considered to occur when $Re < 2000$. However, the transition from laminar to turbulent flow is not a sharp boundary but rather a gradual process, and localized non-persistent turbulences are observed in fluids predominantly characterized as laminar. Table 1 summarizes the thermophysical properties used to calculate Re characteristic of the melt pool length, as well as its value for liquid Al, liquid Cu, and liquid $Al_{83}Cu_{17}$ (eutectic composition) at their melting temperatures. Based on the aforementioned criteria, the flow regime for both elements and the mixture can be classified as predominantly laminar. Still, vortex-like patterns and transient hydrodynamic instabilities are observed, indicating the onset of non-steady-state flow behavior. However, the threshold for the transition from laminar to turbulent flow varies significantly depending on the geometry of the fluid flow, e.g., for plane-Couette geometry, the flow transition can occur at $Re = 400$. In the context of laser melting, numerical simulations often assume incompressible and laminar flow. Despite these assumptions, these models are still able to capture the main features of the fluid flow and transient phenomena [32,34,55], suggesting that the fluid flow regime is indeed predominantly laminar. Nonetheless, discrepancies can be observed between experimental observations (velocity, chemical redistribution, and bubble evolution) and these models. While these discrepancies have been occasionally attributed to the omission of fluid turbulence in the models [56,57], they can also arise from numerous factors, such as inaccurate knowledge of the thermophysical properties of the investigated materials. A numerical direct-energy-deposition simulation suggested that turbulence should be accounted for when $Re > 200$, with the transition to a fully turbulent state occurring between $Re = 540$ and $Re = 900$.[1] In addition, this study highlighted that the turbulent regime is more beneficial for enhancing mixing. Therefore, although Reynolds number is a powerful tool to characterize flow regime, care must be considered when applying it to AM processing considering the lack of characterization. Experimental and simulation works are required to better understand flow regimes in the context of AM.

[1] Note that the Re equation used in Ref. [40] differs by a factor of two with the one used in the current study. As such, values from the Ref. [40] were multiplied by the same factor to facilitate comparison.

Across different length scales, multiple interacting mechanisms govern the mixing of Cu into Al during the AM process. The presence of composition and temperature gradients within the melt pool leads to variations in surface tension. To characterize the effect of surface tension relative to inertial forces and viscous forces in the liquid, the Weber (We) and the Marangoni (Ma) numbers are introduced, as described in [14]:

$$We = \frac{\rho v^2 (L/2)}{\gamma} \tag{2}$$

$$Ma = -\frac{d\gamma}{dT}\frac{L\Delta T}{\mu \alpha_T} \tag{3}$$

where ρ is the liquid density, v is the flow velocity, L is the melt pool length, γ is the surface tension, $d\gamma/dT$ is the surface tension gradient with respect to the temperature, ΔT is the temperature difference between the boiling and melting points, μ is the dynamic viscosity of the liquid, and α_T is the thermal diffusivity of the liquid. Inertial forces dominate when $We > 1$, while surface tension force dominate when $We < 1$. Viscous forces dominate when $Ma < 1$, while surface tension forces dominate when $Ma > 1$. The thermophysical properties used to calculate We and Ma, as well as their values for liquid Al, liquid Cu, and liquid $Al_{83}Cu_{17}$ at the melting temperature, are shown in Table 1.

For Al and Cu, Weber numbers are smaller and larger than 1, respectively. This suggests that surface tension forces dominate over inertial forces for low Cu compositions, while the opposite is true for high Cu compositions. As the composition of Cu in the liquid changes, a transition from surface tension-dominated to inertial force-dominated behavior would be observed. However, the Weber numbers for both elements are relatively close to 1, indicating that surface tension forces and inertial forces are of comparable magnitude and may balance. Estimations of the Marangoni numbers yield values much greater than 1, indicating that surface tension forces dominate over viscous forces and contribute to mass transport within the melt pool. It should be noted that the thermophysical properties reported in Table 1 vary with Cu composition and temperature [58–62], meaning that the results presented here are estimates. Nonetheless, the order of magnitude is captured.

Due to the large density contrast between the two elements ($\rho_{Cu}/\rho_{Al} \approx 3.3$), the gravitational forces involved in the process of

Table 1
Reynolds (Re), Weber (We), Marangoni (Ma), and Galilei (Ga) numbers and the thermophysical properties of liquid Al, liquid Cu, and liquid $Al_{83}Cu_{17}$ at melting temperature used for the calculations. The thermophysical properties were extracted from [58–62]. Superscript $*$ indicates that rule of mixture was used to estimate the thermophysical properties. The dimensionless numbers were rounded.

Liquid	ρ_{T_m} [kg m^{-3}]	T_m [K]	T_b [K]	γ [N m^{-1}]	$d\gamma/dT$ 10^{-4} [N m^{-1} K^{-1}]	μ 10^{-3} [Pa s^{-1}]	α_T 10^{-5} [m^2 s^{-1}]	Re	We	Ma	Ga
Al	2380	933	2743	0.87	−1.55	1.38	3.309	862	0.46	3072	456
Cu	8000	1356	2835	1.30	−2.64	4.38	3.62	913	2.3	1231	511
$Al_{83}Cu_{17}$	3239	825	2759*	0.941	−1.61	~1.97	3.36*	822	0.86	2352	414

mixing must be addressed. To do so, the Froude (Fr) number is used to compare the effects of inertial forces relative to gravitational forces within a flow:

$$Fr = \frac{v}{\sqrt{gH}} \tag{4}$$

where v is the flow velocity, H is the depth of the flow set at 250×10^{-6} m (see Fig. 2), and g is the acceleration due to gravity set at 9.81 m s^{-2}. Inertial forces dominate when $Fr > 1$, while gravitational forces dominate when $Fr < 1$. Using $v = 1$ m s^{-1}, the Froude number is estimated to be approximately $Fr = 20.2$. The flow can therefore be characterized as supercritical, indicating that inertial forces dominate over gravitational forces. The relatively small contribution of gravitational forces, despite the large density difference between the two base materials, is consistent with a previous study [14].

Furthermore, the gravitational forces — which are closely related to the buoyancy forces — can be compared to the viscous forces using the Galilei (Ga) number:

$$Ga = \frac{gH^3}{(\mu/\rho)^2} \tag{5}$$

Galilei numbers for liquid Al, liquid Cu, and liquid $Al_{83}Cu_{17}$ are listed in Table 1. Gravitational forces dominate when $Ga > 1$, while viscous forces dominate when $Ga < 1$. For the investigated liquids, the Galilei numbers are well above 1, suggesting that gravitational forces play a larger role than viscous forces.

Mass transport can be further facilitated by diffusion, although the extent of its contribution depends on the diffusion coefficients of Cu in Al and vice versa. Contrasting conclusions on the subject can be found in the literature, where diffusion is sometimes considered negligible [34] and in other cases non-negligible [31]. These conclusions strongly depend on the choice of the diffusion coefficient which can vary by several orders of magnitude. The experimentally reported order of magnitude of copper diffusion coefficients in aluminum is approximately $D^L_{\mathrm{Cu-Al}} = 5 \times 10^{-9}$ m^2 s^{-1} [63,64]. Considering the upper bound of the melt pool lifetime in the present work ($t_{\mathrm{MP}} = L/\text{scanning speed} = 10^{-3}$ s) and $D^L_{\mathrm{Cu-Al}} = 5 \times 10^{-9}$ m^2 s^{-1}, the diffusion length (l) of Cu in Al in the liquid state can be estimated using $l = \left(2t_{\mathrm{MP}} D^L_{\mathrm{Cu-Al}}\right)^{1/2}$. The calculated diffusion length is approximately $l \sim 3.2$ μm which is more than two orders of magnitude smaller than the maximum melt pool length. This implies that solute transport by diffusion is negligible at the melt pool scale. To further assess the relative importance of fluid flow over diffusion in mixing, the Péclet (Pe) number can be used:

$$Pe = \frac{vL}{D^L_{\mathrm{Cu-Al}}} \tag{6}$$

Fluid flow (advection) dominates when $Pe > 1$, while diffusion dominates when $Pe < 1$. Using the aforementioned values, the Péclet number is calculated to be approximately 10^5, indicating that fluid flow is the primary mechanism of mixing and diffusion remains a secondary mechanism in AM processes.

Finally, to assess the importance of viscous forces over diffusion and fulfill the analysis, the Schmidt (Sc) number is estimated. The Schmidt number is defined as $Sc = Pe/Re$. Using $Pe = 10^5$ and $Re \sim 10^3$ (see Table 1), Sc reads 10^2 indicating that viscous forces dominate over diffusion.

It should be recalled that the maximum flow velocity was used for these calculations, leading to upper bound estimates for the corresponding dimensionless numbers. Experimental observations, however, indicate that the melt pool flow velocity is heterogeneous and, for a given event, decreases over time. Consequently, for the velocity-dependent characteristic numbers — Re, We, Fr, Pe, and Sc — their magnitudes decrease and tend toward zero as the velocity approaches zero. The transitions between dominant mechanisms occurs at velocities below 5×10^{-2} m s^{-1}: approximately 10^{-3}, 5×10^{-2}, 10^{-5}, and 10^{-2} m s^{-1} for Re, Fr, Pe, and Sc, respectively. For the We number, the transition occurs between 0.65 m s^{-1} to 1.46 m s^{-1}, depending on composition, as reported earlier. Thus, surface tension, gravitational forces, and diffusion dominate over fluid flow, inertial, and viscous forces only toward the end of solidification.

During solidification, the composition gradient dictates the local solidification pathway, affecting the liquidus and solidus temperatures (Fig. 5a). The exothermic nature of solidification releases latent heat, locally increasing the temperature. The amount of heat released is composition-dependent [65], meaning it varies spatially in multimaterial systems. Despite the high cooling rates characteristic of LPBF, solute redistribution between the solid and liquid phases is still observed, leading to localized variations in temperature and composition along the solidification front. These in turn influence phase stability throughout the printed track [29,66].

Additionally, factors such as the formation and evolution of bubbles and keyholes, the presence of solid and mushy zones, and recoil pressure effects significantly impact liquid flow dynamics in the melt pool, e.g., the effect of recoil pressure has been shown to be similar to the inertial forces [14]. These interactions underscore the complex nature of fluid and solute transport in multimaterial AM, distinguishing it from conventional monolithic material processing. However, based on the present analysis, the mechanisms acting on mass transport in the melt pool during additive manufacturing of multimaterial can be ranked by degree of importance. Following a top down ranking: surface tension and inertial forces, buoyancy and gravitational forces, viscous forces, and finally diffusion.

The mechanisms governing AM are inherently complex, particularly in the formation and evolution of fluid flow dynamics within the melt pool. These flows are not only driven by intrinsic material properties but are also strongly influenced by processing parameters. To quantitatively assess the contribution of each mechanism involved in Cu–Al mixing during AM, high-resolution, physics-based numerical models are essential. Additionally, a more comprehensive understanding of the thermophysical properties of the materials is required, such as the diffusion coefficients and surface tensions in the liquid phase as a function of the composition and temperature. The present findings provide crucial experimental ground truths for the development and validation of such numerical models, facilitating more accurate predictions of solute redistribution in multimaterial AM.

Beyond the incorporation of freshly added Cu during layer deposition, remelting and remixing of previously solidified layers are also observed. This behavior, expected due to successive laser passes, is highlighted by the blue arrows in Fig. 2a1 (initial state) and Fig. 2a8 (final state after mixing). In contrast, pink arrows indicate the presence of an unmelted Cu particle adhered to the glassy carbon window, where no melting or remixing occurs. For clarity, the presentation of the

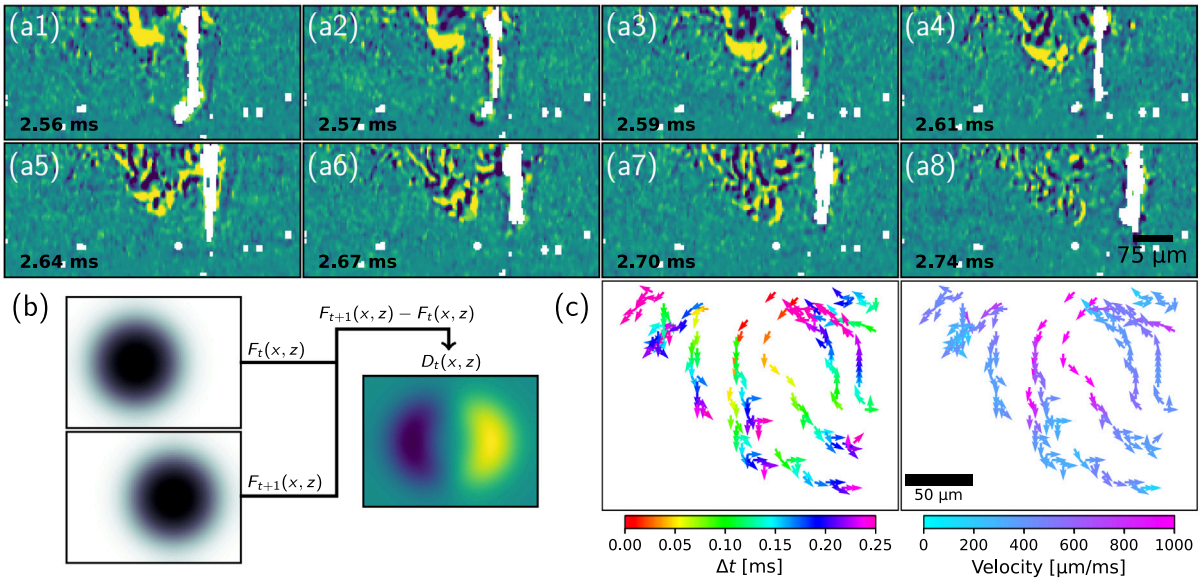

Fig. 3. Characterization of the dynamics and fragmentation of a Cu event during AM: (a) Snapshots of projected (x–z) image differencing during the printing of L4, the image differencing method is schematically presented in (b). (c) Projected relative times and velocities of Cu mixing discrete occurrence for L4 in the melt pool onto the x–z plane.

results and their discussion focused on the addition of the fourth layer, as similar mixing phenomena were consistently observed across all deposited layers. The raw data are provided in Supplementary Videos 1–4 for further analysis.

3.2. Three dimensional Cu distribution

Fig. 4 presents the local Cu composition obtained from microtomography experiments, conducted with a $0.6 \times 0.6 \times 0.6$ µm^3 voxel size, on additional samples with varying numbers of layer additions. The volume renderings (Fig. 4a–d) of the third layer reveal the morphology and Cu distribution within the melted region. A composition projection along the y-axis confirms consistency with the Cu distribution observed in operando imaging experiments. A composition-based thresholding approach (Fig. 4c and Fig. 4d) highlights that the Cu composition primarily ranges between >0 wt Cu and ~ 0.547 wt Cu, corresponding to θ-Al_2Cu. This composition interval accounts for 97%–98% of the melted track volume and spans the biphase region between α-Al and θ-Al_2Cu, as defined by the Al–Cu phase diagram (Fig. 5a). Additionally, a disconnected Cu-rich network with compositions exceeding that of Al_2Cu is observed, representing the remaining volume fraction. The non-uniform distribution of these Cu-rich regions along the track further underscores the stochastic nature of mixing during LPBF.

Fig. 4e provides cross-sectional views of the first three deposited layers. Due to the high solidification rates and limited solute diffusion in the solid state, the final chemical distribution reflects the complex fluid flow dynamics occurring prior to solidification. Additionally, keyhole-induced porosity and shrinkage pores are visible (see Supplementary Videos 1–4). The Cu concentration progressively increases with the number of added layers, exhibiting a gradual compositional transition. This trend is further confirmed in Fig. 4f, which depicts the Cu composition distribution alongside the mean composition (red lines). The Cu composition cumulative distributions are presented in Supplementary Figure 2. Furthermore, a bimodal Cu distribution is evident in layers L2 and L3. At the lower Cu composition range, the distribution stabilizes around $\sim 0.08 - -0.1$ wt, while at higher Cu concentrations, a second peak emerges at $\sim 0.28 - -0.33$ wt. The high probability observed in the first composition range is partially attributed to Cu content thresholding and experimental noise.

To quantify the degree of mixing between Cu and Al in the melted regions (as shown in Fig. 4c), a normalized total entropy of mixing index (Σ_{tot}) [67] is introduced, defined as:

$$\Sigma_{tot} = \frac{S_{tot}}{S_{tot,P}} = \frac{1/b \sum_{i=1}^{b} -p_i \log(p_i) - (1-p_i)\log(1-p_i)}{-P\log(P) - (1-P)\log(1-P)} \tag{7}$$

where b is the number of voxel, p_i the Cu composition in the voxel i, and P the average Cu composition of a given set of layer addition. The index ranges from 0 to 1, where 1 indicates perfectly ordered and 0 completely unmixed states (Fig. 4g). In this study, Σ_{tot} characterizes mesoscale heterogeneity, where different phase compositions — such as those in a eutectic microstructure — are averaged. The results indicate that as the number of layer additions increases, the overall composition homogeneity remains stable in the solidified volume. The small variation observed, e.g., L2, are likely due to the intrinsic variability of the AM process, as the microtomography experiments were conducted on additional samples.

3.3. Solidified microstructure

Based on the Cu distribution observed in Fig. 4 and the Al–Cu equilibrium phase diagram (Fig. 5a), the solidified microstructure is expected to primarily consist of α-Al and θ-Al_2Cu phases, with minor fractions of Cu-rich phases. This expectation is validated by the XRD profile of L4 (Fig. 5b), which confirms that α-Al and θ-Al_2Cu are the dominant constituents. In addition to these primary phases, η-AlCu and ω-Cu phases are also detected, albeit in smaller fractions. The ω-Cu peaks are attributed to Cu-rich regions, likely formed due to partially molten Cu particles and incomplete mixing within the melt pool. Additionally, supersaturated ω-Cu is expected, likely resulting from rapid cooling conditions during solidification [68]. The η-AlCu phases is presumed to form at interfaces between Cu-rich regions and eutectic microstructures [69,70]. Furthermore, additional Cu-rich phases with compositions spanning from η-AlCu to ω-Cu may be present; however, their volume fractions are too low to be distinctly resolved by XRD analysis.

Fig. 5c–f present scanning electron microscopy secondary electron (SEM-SE) images and energy-dispersive X-ray spectroscopy (EDX) maps of Al and Cu, revealing the solidified microstructure of L3 along the y–z plane. These images distinguish two distinct microstructural regions: (i)

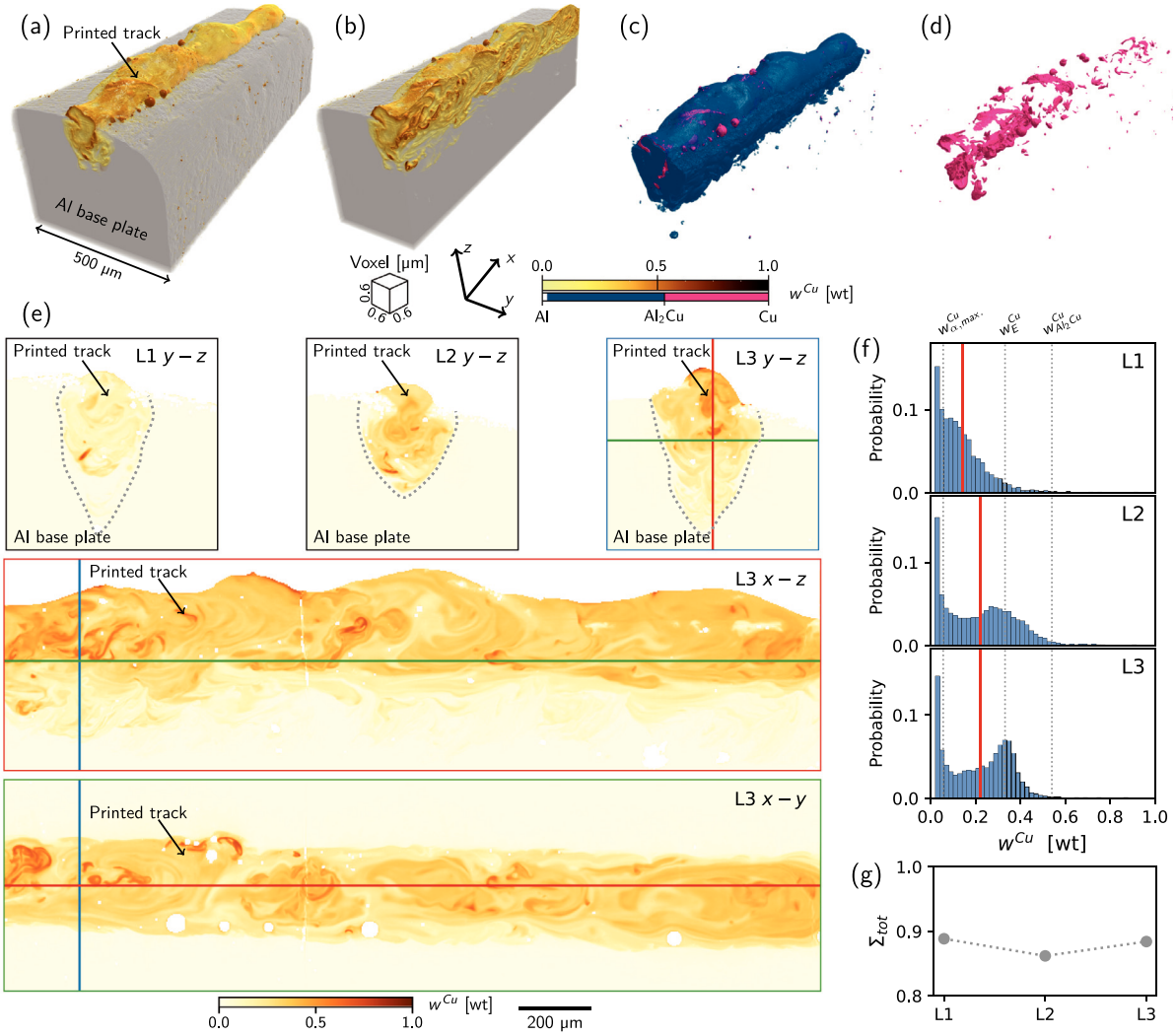

Fig. 4. Three dimensional characterization of the solidified Cu distribution. Volume renderings of sample L4: (a) full sample volume, (b) cross-section through the track, (c) regions with Cu composition above 0.05 wt, and (d) region with Cu composition above Al_2Cu composition, i.e., ~0.5407 wt Cu. Panel (e) contains y–z cross-section views of L1, L2, and L3, and x–z and x–y cross-section views of L3. (f) Distribution of Cu composition and mean Cu composition (red lines) and (g) normalized total entropy of mixing index (Σ_{tot}) after the addition of each layer. A minimum threshold of 0.02 wt Cu has been used to remove the Al matrix contribution for (f and g). Vertical dotted lines in (f) show the maximum solubility in Al, the eutectic point composition, and the Al_2Cu phases composition in Cu, $w^{Cu}_{\alpha,max.}$, w^{Cu}_{E}, and $w^{Cu}_{Al_2Cu}$, respectively. A minimum threshold of 0.05 wt Cu was applied in (c) to enhance readability. Frames with blue, red, or green color for L3 specify cross-section positions. The laser traveled along the x direction. Color scales represent the Cu composition in weight and the dotted lines represent the approximate position of the interfaces.

darker contrast areas, corresponding to α-Al primary dendrites, and (ii) lighter contrast areas, representing a lamellar eutectic microstructure composed of $\alpha - \theta$ phases. Quantitative analysis of the images yields a secondary dendrite arm spacing ($SDAS$) of 0.443 ± 0.028 µm and an interlamellar spacing (λ) of 0.047 ± 0.002 µm. As expected, the dendritic regions exhibit a lower Cu content than the eutectic microstructure, as confirmed by Fig. 5f1 and Fig. 5f2. However, the presented composition maps should be interpreted qualitatively, as the interaction volume of the EDX measurement significantly exceeds the microstructural length scales [71].

The bimodal Cu composition distribution observed in microtomography experiments (Fig. 4) can be directly correlated with these microstructural features. The first and second composition peaks correspond to regions primarily consisting of α-Al dendrites and the eutectic microstructure, respectively. Given the high solidification rates characteristic of LPBF, α-Al is expected to be supersaturated with Cu, as indicated by both EDX maps and Cu distribution data [72,73]. Additionally, a lamellar eutectic microstructure is observed in interdendritic regions. Notably, θ-Al_2Cu dendrites are absent, which can be attributed to two possible mechanisms. The first, albeit unlikely, is that the local Cu concentration in the melt pool remained hypoeutectic during solidification (Fig. 5a).

However, this hypothesis is contradicted by the results in Fig. 4f, which show that the composition exceeds the eutectic composition. This deviation from equilibrium expectations, where hypereutectic compositions should initiate solidification with Al_2Cu, is attributed to the rapid solidification conditions inherent to additive manufacturing. Under rapid solidification, the solidification front velocity becomes sufficiently high that diffusion length becomes smaller that the characteristic size of the microstructure or interface width, leading to solute trapping. As a result, the degree of solute partitioning decreases at the solid/liquid interface and solute can exceed the solid solubility given by equilibrium. This effect is characterized by a rate-dependent partition coefficient $k(R)$, which tends to unity as interface velocity increases. At $k(R) = 1$, partitionless solidification occurs, i.e., both the solid and liquid phases share the same composition. The thermodynamic path then nearly follows the T_0 line which represents equal Gibbs free energy of the two phases. Consequent to the decrease of partitioning,

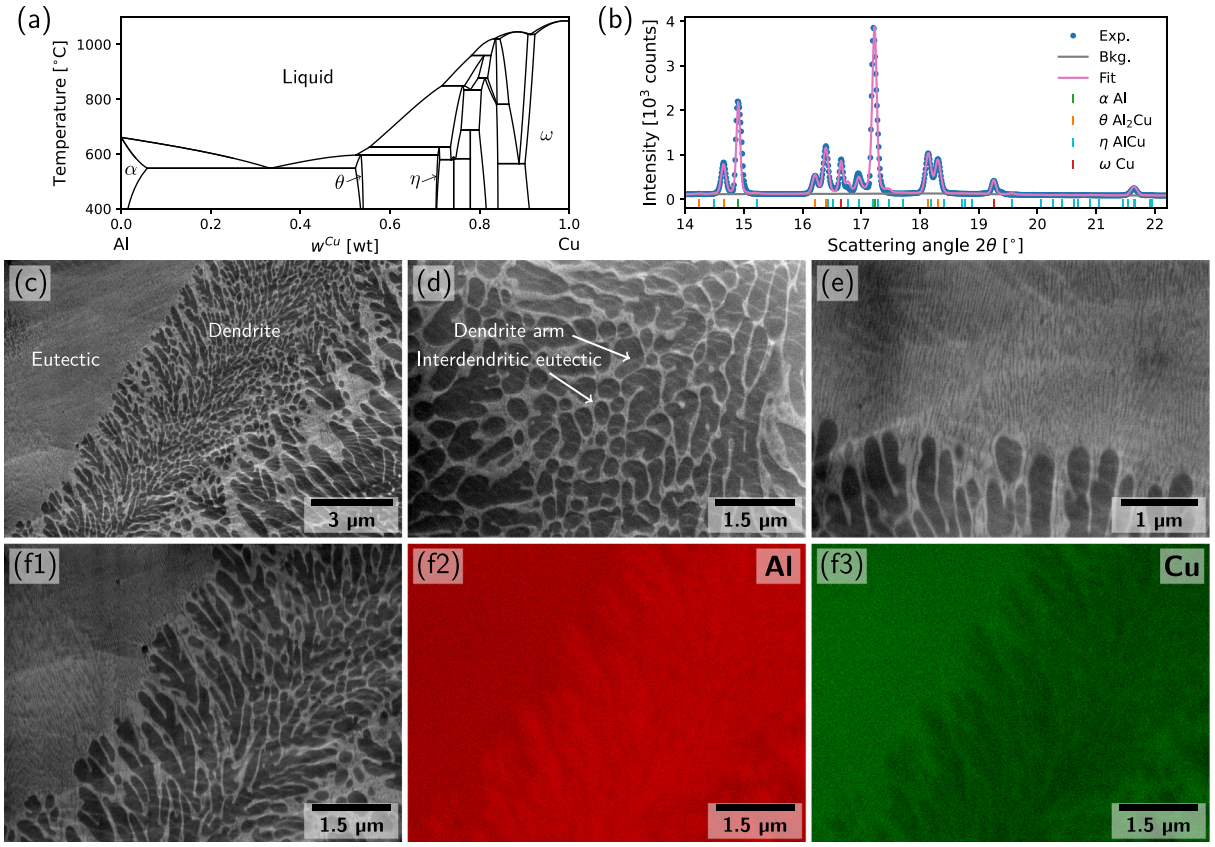

Fig. 5. Microstructural characterization of the solidified Al–Cu multimaterial along the y–z plane with the vertical of the images aligned with z. (a) Al–Cu equilibrium binary phase diagram, (b) X-ray diffraction profile and indexed phases, (c–e) SEM-SE images, and (f) SEM-SE image and EDX elemental maps of Al and Cu. The interaction depth between an electron beam at an accelerating voltage of 10 kV with a bulk pure Al sample is ~1.3 μm [71]. Additional SEM-SE images taken from various positions across the y–z plane are provided in Supplementary Figure 3.

the undercooling at the interface increases—the interface temperature decreases.

Since the solidification and growth rate of dendritic, planar, or eutectic microstructures are different, there is a competition between phases. Applying the criterion of maximum growth temperature, which states that the phase with a higher solid/liquid interface temperature at a given growth velocity has a higher driving force to form, it is possible to predict which phase will form for given compositions and growth velocities [29,74–76].

The θ-Al_2Cu phase is an intermetallic phase with a layered and chemically ordered tetragonal crystal structure. It has a steep solidus and T_0 slopes and a narrow composition range (32.1 at% to 33.6 at% of Cu) [68]. This makes θ-phase less capable of accommodating solute trapping compared to α-phase, even for high growth velocities. Therefore, under high solidification rates, the θ-phase requires significantly more undercooling to nucleate and grow. The required undercooling to form Al_2Cu, which is dominated by the solute undercooling component, can exceed that of eutectic or α-phases. Therefore, only a limited range of solidification interface velocities allows for θ-Al_2Cu phase to form and grow upon rapid solidification. As an example, in a hypereutectic Al–37wt%Cu alloy, the maximum expected growth rates for the dendritic θ-phase to form is $R = 0.0357$ m s^{-1} [77]. As a result of this restricted solidification window, the eutectic growth domain — comprising α-Al and θ-Al_2Cu — expands in composition, a phenomenon consistent with previous studies on rapid solidification [29,66,74,76].

Finally, in AM, thermal gradients (G) and cooling rates ($\dot{T} = GR$) vary over space and time within the melt pool. As a consequence, solidification rates are heterogeneous across it. This ultimately results into spatially varying microstructures. In multimaterial AM, an additional gradient in composition further complicates the system. In such systems, the interplay between velocity, composition, and local thermodynamic conditions can create local conditions allowing the coexistence, at a larger scale, of dendritic and eutectic phases.

The mean solidification growth rate can be estimated using empirical relationships: $SDAS = 35R_\alpha^{2/3}$ for α-Al dendrites [78] and $\lambda^2 R_E = 99$ for $\alpha - \theta$ lamellar eutectic [79]. To differentiate between these two growth rates, subscripts α and E are assigned to α-Al dendrites and $\alpha - \theta$ lamellar eutectic, respectively. The estimated values are $R_\alpha \sim 0.69$ m s^{-1} and $R_E \sim 0.045$ m s^{-1}. By correlating these growth rates with microtomography-based composition measurements (Fig. 4f), the observed microstructures align well with predictions from monolithic composition alloy systems [29,66]. Furthermore, the calculated R_E supports the absence of θ-phase dendrites, consistent with prior studies on binary Al–Cu alloys processed under rapid solidification conditions [29,66,74]. It should be noted that the empirical coefficients linking $SDAS$ to $R_\alpha^{2/3}$ [78] do not fully encompass the high solidification rates observed in this study, requiring extrapolation beyond their reported range. Additionally, these coefficients depend on Cu content, and variations in published values exist. Here, the most recent upper-bound coefficient is applied [78].

The mean normal solidification rate at the trailing melt pool boundary provides a first-order comparison to these calculated values. Based on real-time imaging data, this rate was estimated using the equation: $R_{AM} = V\cos(\langle\phi\rangle)$, where V represents the scanning speed, and $\langle\phi\rangle \approx 53°$ denotes the angle between the scanning direction and the normal to the trailing melt pool boundary. This yields R_{AM} ~300 mm s^{-1}, which is more than twice lower than R_α. Despite this discrepancy, the predicted microstructure remains consistent with previous literature [29,66]. However, these findings underscore the lack of a robust

correlation between solidification rates and microstructural scaling laws in the context of rapid solidification in AM [78,80].

Microhardness testing performed on the sample cross-section (Supplementary Figure 4) showed an increase of hardness with higher Cu contents, as expected. Maximum microhardness reached approximately 1000 Hv, compared to an average of 32 Hv for pure Al or approximately 120 Hv for LPBF-manufactured CuCrZr [81]. However, this increase is primarily attributed to the microstructural refinement — specifically, the reduction of interlamellar spacing — rather than composition alone. Using the Hall–Petch relationship provided in [82] for an Al–Cu eutectic composition, the estimated hardness using $\lambda = 0.047$ µm is approximately 790 Hv, showing good agreement with our measurements. The remaining difference can be attributed to compositional variations (solid solution strengthening) and the extrapolation of the relationship beyond its originally validated range. Additionally, it is well known that mechanical properties in crystalline solids exhibit a size dependence relatives to the applied load and indenter, smaller being stronger [83]. In the context of hardness measurements, this phenomenon is referred as the *indentation size effect*. Consequently, the maximum microhardness values reported in this study should be interpreted with care. Such sharp changes in mechanical properties are likely to induce stress redistribution at the Al–CuCrZr interface under mechanical loading, potentially leading to localized deformation or crack initiation. Finally, these high hardness levels, combined with differences in physical properties and the inherent temperature gradients observed during multimaterial AM, promote crack formation during cooling [42]. For instance, a crack across the solidified melt pool (y–z) is visible in Fig. 4e.

These results suggest that the local solidification behavior in multimaterial systems can be effectively understood using principles derived from monolithic composition alloys. Furthermore, processing maps linking composition and growth rates to final microstructure could serve as a preliminary predictive tool for multimaterial numerical simulations. Such models could enable the estimation of physicochemical and mechanical properties, thus maximizing the design flexibility of AM.

4. Summary and outlook

This study characterized in real-time the mixing of elements in the melt pool of Al–Cu multimaterials during LPBF process, leveraging X-ray attenuation measurements. The results reveal complex solute transport mechanisms, driven by material properties, fluid flow dynamics, keyhole evolution, and bubble formation, all of which influence mixing at multiple length scales. Fig. 6 schematically summarizes these key findings.

Cu incorporation was found to occur primarily through discrete transport events at the melt pool surface, particularly on the trailing side and at the keyhole position (Fig. 6a, top panel). As demonstrated, spontaneous wetting cannot occur because the spreading liquid (Cu) has a higher surface tension than the substrate liquid (Al). Therefore, additional dynamic driving forces, such as Marangoni flow or hydrodynamic fluctuations, must assist the process, leading to the stochastic and discrete nature of the incorporation. These events are followed by element redistribution, where successive layer deposition induces remelting and remixing of the underlying track, leading to a progressive increase in compositional homogeneity (Fig. 6a, middle panel). Moreover, chemical heterogeneity at the local scale results in microstructural inhomogeneity, with regions exhibiting distinct phase compositions (Fig. 6a, bottom panel). Fig. 6b highlights that surface tension, inertial forces, and recoil pressure play a primary role in mass transport for the majority of the melt pool lifetime and thus in the mixing of multimaterial processed using AM.

The mode of incorporation observed here is consistent with studies performed on the same system [41] and on other multimaterial systems during additive manufacturing, namely In718 powder onto Al base plate and 316L powder onto Al base plate [42]. For the latter, the surface tension gradients of the liquids (considering the pure elements) display the same trend, i.e., the surface tension of the spreading liquid is higher than that of the substrate liquid. Therefore, this could suggest that this mode of incorporation will be expected for systems sharing the same surface tension properties, such as Ti onto Cu, Fe onto Cu, and Ni onto Cu [84]. Conversely, when the surface tension gradient is reversed (e.g., Al onto Cu or Cu onto Fe), spontaneous wetting would occurs, facilitating a more continuous and homogeneous mixing. This underscores the importance of the printing sequence (A on B or B on A) to obtain sound bonds when processing multimaterials [24].

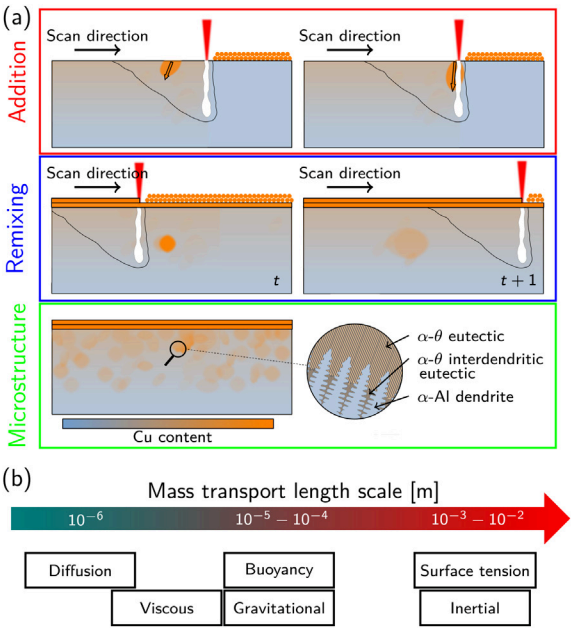

Fig. 6. Schematic outlining (a) the principal phenomena dictating Cu evolution observed during layer additions and the resulting microstructure and (b) the typical length scales of the forces participating to the mass transport in the melt pool.

Furthermore, the thermal mismatch between the high melting temperature of the powder relative to the melting temperature of the base material must be considered. These powder particles initially act as heat sinks which therefore delays their melting relative to the base material. Consequently, their initial incorporation into the melt pool may be driven by their momentum rather than a liquid–liquid mixing process. This ultimately affects the melt pool flow and therefore the distribution of the elements [85].

In addition, it is worth mentioning that alloying elements and contaminants present in the materials or introduced during the process can strongly affect the physical properties of the liquids and therefore change the wetting behavior [84,86]. Although the surface tension evolution is primarily monotonic with the composition in binary systems [86], certain systems, such as Fe–Ti, exhibits local minima or maxima which ultimately influence wetting behavior during mixing. However, the mixing length scales and predominant mechanisms are expected to hold for other multimaterial systems, as the orders of magnitude of the physical constants remain similar.

Finally, although some generalization to other multimaterial systems can made, specificities may arise from differences in processing parameters, thermophysical properties, and phase formation and stability. Notably, significant differences are expected in multimaterial systems presenting a liquid immiscibility. Contrary to the binary Fe–Cu system, where liquid miscible gap disappears above approximately 1450°C—theoretically allowing for unrestricted mixing, the 316L–CuCrZr system exhibits a persistent liquid miscibility gap that

extends well above the melting point of the 316L phase [87]. In such immiscible systems, a distinction must be made between the incorporation event and the subsequent mixing. In both cases, the mixing subsequent to the incorporation and final element distribution are heavily governed by the liquid miscibility gap. However, in 316L–CuCrZr, the persistent miscible gap prevents homogenization of the superheated liquid, causing discrete droplets with vastly different compositions to persist or further segregate during cooling.

Furthermore, higher degrees of homogeneity are expected for high energy density conditions, large melt pool width and depth, and multitracks and interlayer rotation scanning strategies. The increased melt-pool lifetime in these conditions enables mass transport over a wider length scale, promoting better mixing [25]. However, for example, in the case of spiral scanning strategies, gradients of chemical homogeneity from the outer to the inner section of the spiral might be observed if the processing parameters are not adjusted during manufacturing. This scanning strategy could be used to leverage the formation of heterostructured microstructures. To better understand the effect of scanning strategy on element distribution during AM, in situ and operando X-ray tomography experiments have to be exploited [88,89]. However, due to similar X-ray attenuation coefficients at given X-ray energies, some multimaterial systems, such as Fe–Ni and Fe–Cu, do not lend themselves to this type of experiments.

5. Conclusions

Leveraging attenuation measurements, this study employed X-ray radiography and X-ray computed tomography to investigated elemental redistribution during laser powder bed fusion of an Al–CuCrZr multimaterial system. Real-time radiography experiments at 100,000 frames s^{-1} enabled direct observation of the mixing dynamic during the deposition of successive single tracks. The main conclusions are summarized as follow:

- The mixing of CuCrZr into Al occurs through discrete and stochastic events originating from the melt pool surface. This mode of incorporation could results from the poor wetting of the spreading liquid on the substrate liquid, necessitating additional dynamic driving forces to assist the incorporation process. Therefore, these events are driven primarily by melt pool fluid dynamics and may coincide with keyhole collapses.
- The melt pool composition is heterogeneous, typically ranging approximately from Al to Al_2Cu. Upon solidification, this compositional variability leads to the formation of distinct microstructures due to differing solidification paths. The resulting out-of-equilibrium local microstructure can be predicted from monolithic alloy processing–microstructure maps using the local composition and cooling rates.
- The predominant mixing mechanisms and length scales observed in this study are likely generalizable to a wider set of multimaterial systems, with notable differences expected for alloy combinations exhibiting liquid immiscibility, such as 316L–CuCrZr. Additionally, the incorporation mode could be expected to hold for multimaterial systems in which the spreading liquid has a higher surface tension than the substrate liquid. However, due to the metallurgical complexity of multimaterial systems and their interplay with processing conditions, further investigation of diverse multimaterial systems is necessary to fully validate the transferability of these findings across different metallurgical combinations.

This work provides critical ground truth for the development and validation of advanced numerical models, thereby facilitating a deeper understanding of multimaterial AM processes. Beyond numerical modeling, these findings highlight the need for next-generation experimental capabilities, including high-resolution operando imaging, improved spatial and temporal resolution, and real-time tomography. Such advancements will enable a more comprehensive understanding of solute mixing dynamics, ultimately enhancing process control and material design strategies in multimaterial AM.

CRediT authorship contribution statement

Steve Gaudez: Writing – review & editing, Writing – original draft, Methodology, Investigation, Formal analysis, Data curation, Conceptualization. **Andaç Özsoy:** Writing – review & editing, Investigation, Formal analysis. **Yunhui Chen:** Writing – review & editing, Investigation, Formal analysis. **William Hearn:** Writing – review & editing, Investigation. **Alexander Rack:** Writing – review & editing, Resources. **Steven Van Petegem:** Writing – review & editing, Supervision, Resources, Investigation, Funding acquisition.

Declaration of competing interest

The authors declare that they have no known competing financial interests or personal relationships that could have appeared to influence the work reported in this paper.

Acknowledgments

This project has received financial support by the Swiss ETH domain within the Strategic Focus Area (SFA) Advanced Manufacturing SMART-AM project, the Swiss National Science Foundation (SNSF), Switzerland under the grant agreement No. CRSII5_193799, and the European Union's Horizon 2020 research and innovation programme under the Marie Skłodowska-Curie grant agreement No. 884104 (PSI-FELLOW-III-3i). We acknowledge travel funding provided by the International Synchrotron Access Program, Switzerland (ISAP-AS/IA243/23653) managed by the Australian Synchrotron, part of ANSTO, and funded by the Australian Government. We acknowledge the European Synchrotron Radiation Facility (ESRF) for provision of synchrotron radiation facilities under proposal number HC-5951 and MI-1484 and we would like to thank Jean Paul Valade and Diego Hopson Safatli for assistance and support in using beamline ID19. We acknowledge DESY (Hamburg, Germany), a member of the Helmholtz Association HGF, for the provision of experimental facilities. Parts of this research were carried out at PETRA III and we would like to thank Azat Khadiev for assistance in using P23. Beamtime was allocated for proposal I-20231380 EC.

Appendix A. Supplementary data

Supplementary material related to this article can be found online at https://doi.org/10.1016/j.addma.2026.105149.

Data availability

The data that support the findings of this study are available as Supplementary Materials and from the corresponding author upon reasonable request.

References

[1] T. DebRoy, H.L. Wei, J.S. Zuback, T. Mukherjee, J.W. Elmer, J.O. Milewski, A.M. Beese, A. Wilson-Heid, A. De, W. Zhang, Additive manufacturing of metallic components – Process, structure and properties, Prog. Mater. Sci. 92 (2018) 112–224.

[2] W. Gao, Y. Zhang, D. Ramanujan, K. Ramani, Y. Chen, C.B. Williams, C.C. Wang, Y.C. Shin, S. Zhang, P.D. Zavattieri, The status, challenges, and future of additive manufacturing in engineering, Computer-Aided Des. 69 (2015) 65–89.

[3] H. Hassanin, L. Finet, S.C. Cox, P. Jamshidi, L.M. Grover, D.E. Shepherd, O. Addison, M.M. Attallah, Tailoring selective laser melting process for titanium drug-delivering implants with releasing micro-channels, Addit. Manuf. 20 (2018) 144–155.

[4] B. Blakey-Milner, P. Gradl, G. Snedden, M. Brooks, J. Pitot, E. Lopez, M. Leary, F. Berto, A. Du Plessis, Metal additive manufacturing in aerospace: A review, Mater. Des. 209 (2021) 110008.

[5] S. Rouf, A. Malik, N. Singh, A. Raina, N. Naveed, M.I.H. Siddiqui, M.I.U. Haq, Additive manufacturing technologies: Industrial and medical applications, Sustain. Oper. Comput. 3 (2022) 258–274.

[6] Y. Li, Z. Feng, L. Hao, L. Huang, C. Xin, Y. Wang, E. Bilotti, K. Essa, H. Zhang, Z. Li, et al., A review on functionally graded materials and structures via additive manufacturing: from multi-scale design to versatile functional properties, Adv. Mater. Technol. 5 (6) (2020) 1900981.

[7] L. Romero-Resendiz, M. El-Tahawy, T. Zhang, M. Rossi, D. Marulanda-Cardona, T. Yang, V. Amigó-Borrás, Y. Huang, H. Mirzadeh, I. Beyerlein, et al., Heterostructured stainless steel: Properties, current trends, and future perspectives, Mater. Sci. Eng.: R: Rep. 150 (2022) 100691.

[8] S. Tibbits, 4D printing: multi-material shape change, Archit. Des. 84 (1) (2014) 116–121.

[9] S. Gao, Z. Li, S. Van Petegem, J. Ge, S. Goel, J.V. Vas, V. Luzin, Z. Hu, H.L. Seet, D.F. Sanchez, et al., Additive manufacturing of alloys with programmable microstructure and properties, Nat. Commun. 14 (1) (2023) 6752.

[10] A. Bandyopadhyay, B. Heer, Additive manufacturing of multi-material structures, Mater. Sci. Eng.: R: Rep. 129 (2018) 1–16.

[11] D. Wang, L. Liu, G. Deng, C. Deng, Y. Bai, Y. Yang, W. Wu, J. Chen, Y. Liu, Y. Wang, et al., Recent progress on additive manufacturing of multi-material structures with laser powder bed fusion, Virtual Phys. Prototyp. 17 (2) (2022) 329–365.

[12] D. Gu, X. Shi, R. Poprawe, D.L. Bourell, R. Setchi, J. Zhu, Material-structure-performance integrated laser-metal additive manufacturing, Science 372 (6545) (2021) eabg1487.

[13] M.H. Mosallanejad, B. Niroumand, A. Aversa, A. Saboori, In-situ alloying in laser-based additive manufacturing processes: A critical review, J. Alloys Compd. 872 (2021) 159567.

[14] A. Zafari, S.P. Akula, M. Li, A. Wakai, A. Gabourel, S.J. Clark, K. Fezzaa, I. Gibson, A. Moridi, Operando synchrotron X-ray analysis of melt pool dynamics in an Al-Sn immiscible alloy, Addit. Manuf. 103 (2025) 104754.

[15] Z. Kuai, Z. Li, B. Liu, Y. Chen, H. Li, P. Bai, Microstructure and mechanical properties of CuCrZr/316L hybrid components manufactured using selective laser melting, J. Alloys Compd. 955 (2023) 170103.

[16] T. Zhang, Z. Huang, T. Yang, H. Kong, J. Luan, A. Wang, D. Wang, W. Kuo, Y. Wang, C.-T. Liu, In situ design of advanced titanium alloy with concentration modulations by additive manufacturing, Science 374 (6566) (2021) 478–482.

[17] F. Bosio, D. Manfredi, M. Lombardi, Homogenization of an Al alloy processed by laser powder bed fusion in-situ alloying, J. Alloys Compd. 904 (2022) 164079.

[18] S. Marola, D. Gianoglio, F. Bosio, A. Aversa, M. Lorusso, D. Manfredi, M. Lombardi, L. Battezzati, Alloying AlSi10Mg and Cu powders in laser single scan tracks, melt spinning, and laser powder bed fusion, J. Alloys Compd. 821 (2020) 153538.

[19] H. Li, E.G. Brodie, C. Hutchinson, Predicting the chemical homogeneity in Laser Powder Bed Fusion (LPBF) of mixed powders after remelting, Addit. Manuf. 65 (2023) 103447.

[20] H. Fan, Q. Shi, C. Wang, Y. Tian, K. Zhou, S. Yang, Laser powder bed fusion of bimetallic stainless steel/nickel-based superalloy: Interface and mechanical properties, Mater. Sci. Eng.: A 877 (2023) 145193.

[21] J. Zhang, X. Wang, J. Gao, L. Zhang, B. Song, L. Zhang, Y. Yao, J. Lu, Y. Shi, Additive manufacturing of Ti–6Al–4V/Al–Cu–Mg multi-material structures with a Cu interlayer, Int. J. Mech. Sci. 256 (2023) 108477.

[22] C. Wei, L. Liu, Y. Gu, Y. Huang, Q. Chen, Z. Li, L. Li, Multi-material additive-manufacturing of tungsten - copper alloy bimetallic structure with a stainless-steel interlayer and associated bonding mechanisms, Addit. Manuf. 50 (2022) 102574.

[23] J. Preis, Z. Wang, J. Howard, Y. Lu, N. Wannenmacher, S. Shen, B.K. Paul, S. Pasebani, Effect of laser power and deposition sequence on microstructure of GRCop42 - Inconel 625 joints fabricated using laser directed energy deposition, Mater. Des. 241 (2024) 112944.

[24] C. Wang, Y. Wang, H. Fan, Y. Sun, S. Yang, Crack-free nickel-copper (Monel K500/GRCop-42) interfaces formed under alternating build sequences via multi-material laser powder bed fusion, Addit. Manuf. 114 (2025) 105037.

[25] J. Chen, Y. Yang, C. Song, D. Wang, S. Wu, M. Zhang, Influence mechanism of process parameters on the interfacial characterization of selective laser melting 316L/CuSn10, Mater. Sci. Eng.: A 792 (2020) 139316.

[26] J. Elmer, S. Allen, T. Eagar, Microstructural development during solidification of stainless steel alloys, Met. Trans. A 20 (1989) 2117–2131.

[27] Z. Hu, Z. Ma, L. Yu, Y. Liu, Functionally graded materials with grain-size gradients and heterogeneous microstructures achieved by additive manufacturing, Scr. Mater. 226 (2023) 115197.

[28] S. Sumarli, F. Malamud, S. Van Petegem, S. Gaudez, A. Baganis, M. Busi, E. Polatidis, C. Leinenbach, R.E. Logé, M. Strobl, Operando phase mapping in multi-material laser powder bed fusion, Virtual Phys. Prototyp. 19 (1) (2024) e2429132.

[29] S. Gill, W. Kurz, Rapidly solidified Al–Cu alloys–I. experimental determination of the microstructure selection map, Acta Met. et Mater. 41 (12) (1993) 3563–3573.

[30] H. Li, S. Thomas, C. Hutchinson, Delivering microstructural complexity to additively manufactured metals through controlled mesoscale chemical heterogeneity, Acta Mater. 226 (2022) 117637.

[31] V.E. Küng, R. Scherr, M. Markl, C. Körner, Multi-material model for the simulation of powder bed fusion additive manufacturing, Comput. Mater. Sci. 194 (2021) 110415.

[32] L. Yao, S. Huang, U. Ramamurty, Z. Xiao, On the formation of "Fish-scale" morphology with curved grain interfacial microstructures during selective laser melting of dissimilar alloys, Acta Mater. 220 (2021) 117331.

[33] C. Tang, L. Yao, H. Du, Computational framework for the simulation of multi material laser powder bed fusion, Int. J. Heat Mass Transfer 191 (2022) 122855.

[34] A. Chouhan, M. Hesselmann, A. Toenjes, L. Mädler, N. Ellendt, Numerical modelling of in-situ alloying of Al and Cu using the laser powder bed fusion process: A study on the effect of energy density and remelting on deposited track homogeneity, Addit. Manuf. 59 (2022) 103179.

[35] A. Samaei, Z. Sang, J.A. Glerum, J.-E. Mogonye, G.J. Wagner, Multiphysics modeling of mixing and material transport in additive manufacturing with multicomponent powder beds, Addit. Manuf. 67 (2023) 103481.

[36] M. Afrasiabi, M. Bambach, Modelling and simulation of metal additive manufacturing processes with particle methods: A review, Virtual Phys. Prototyp. 18 (1) (2023) e2274494.

[37] S. Ghosh, J. Zollinger, M. Zaloznik, D. Banerjee, C.K. Newman, R. Arroyave, Modeling of hierarchical solidification microstructures in metal additive manufacturing: Challenges and opportunities, Addit. Manuf. 78 (2023) 103845.

[38] N. Ren, J. Li, R. Zhang, C. Panwisawas, M. Xia, H. Dong, J. Li, Solute trapping and non-equilibrium microstructure during rapid solidification of additive manufacturing, Nat. Commun. 14 (1) (2023) 7990.

[39] L. Wang, Z. Guo, G. Peng, S. Wu, Y. Zhang, W. Yan, Evaporation-induced composition evolution in metal additive manufacturing, Adv. Funct. Mater. (2024) 2412071.

[40] V. Jacquier, J. Zollinger, P. Zeller, M. Dal, F. Schuster, H. Maskrot, W. Pacquentin, Melt pool turbulence effects on the interface between dissimilar materials manufactured by directed energy deposition with laser and powder, J. Mater. Eng. Perform. 30 (2021) 8810–8820.

[41] X. Zhang, Z. Tang, Q. Wei, A. Wang, M. Wang, H. Sun, Y. Wu, C. Xia, M. Qian, H. Wang, H. Wang, High-throughput screening of process parameters and composition in laser additive manufacturing via in-situ X-ray imaging, Scr. Mater. 263 (2025) 116681.

[42] J. Xu, D. Cheng, X. Li, H. Gu, W. Li, C. Lu, X. Yang, L. Li, C. Wei, Revealing the interplay between element mixing, intermetallics, and microcracks in multi-material laser additive manufacturing, Addit. Manuf. 111 (2025) 104971.

[43] S.L. Sing, L.P. Lam, D.Q. Zhang, Z.H. Liu, C.K. Chua, Interfacial characterization of SLM parts in multi-material processing: Intermetallic phase formation between AlSi10Mg and C18400 copper alloy, Mater. Charact. 107 (2015) 220–227.

[44] J.H. Martin, B.D. Yahata, J.M. Hundley, J.A. Mayer, T.A. Schaedler, T.M. Pollock, 3D printing of high-strength aluminium alloys, Nature 549 (7672) (2017) 365–369.

[45] S. Dhara, A. Das, Impact of ultrasonic welding on multi-layered Al–Cu joint for electric vehicle battery applications: A layer-wise microstructural analysis, Mater. Sci. Eng.: A 791 (2020) 139795.

[46] Z. Wang, X. Lin, L. Wang, Y. Cao, Y. Zhou, W. Huang, Microstructure evolution and mechanical properties of the wire + arc additive manufacturing Al-Cu alloy, Addit. Manuf. 47 (2021) 102298.

[47] S. Hocine, S. Van Petegem, U. Frommherz, G. Tinti, N. Casati, D. Grolimund, H. Van Swygenhoven, A miniaturized selective laser melting device for operando X-ray diffraction studies, Addit. Manuf. 34 (2020) 101194.

[48] W. Mirihanage, K.V. Falch, I. Snigireva, A. Snigirev, Y. Li, L. Arnberg, R. Mathiesen, Retrieval of three-dimensional spatial information from fast in situ two-dimensional synchrotron radiography of solidification microstructure evolution, Acta Mater. 81 (2014) 241–247.

[49] E. Liotti, C. Arteta, A. Zisserman, A. Lui, V. Lempitsky, P.S. Grant, Crystal nucleation in metallic alloys using X-ray radiography and machine learning, Sci. Adv. 4 (4) (2018) eaar4004.

[50] J. Kieffer, V. Valls, N. Blanc, C. Hennig, New tools for calibrating diffraction setups, J. Synchrotron Radiat. 27 (2) (2020) 558–566.

[51] B.H. Toby, R.B. Von Dreele, GSAS-II: the genesis of a modern open-source all purpose crystallography software package, J. Appl. Crystallogr. 46 (2) (2013) 544–549.

[52] A. Singh, Review article digital change detection techniques using remotely-sensed data, Int. J. Remote Sens. 10 (6) (1989) 989–1003.

[53] M. Bayat, A. Thanki, S. Mohanty, A. Witvrouw, S. Yang, J. Thorborg, N.S. Tiedje, J.H. Hattel, Keyhole-induced porosities in laser-based powder bed fusion (L-PBF) of Ti6Al4V: High-fidelity modelling and experimental validation, Addit. Manuf. 30 (2019) 100835.

[54] J. Yang, L.M. Schlenger, M.H. Nasab, S. Van Petegem, F. Marone, R.E. Logé, C. Leinenbach, Experimental quantification of inward marangoni convection and its impact on keyhole threshold in laser powder bed fusion of stainless steel, Addit. Manuf. 84 (2024) 104092.

[55] P.S. Cook, A.B. Murphy, Simulation of melt pool behaviour during additive manufacturing: Underlying physics and progress, Addit. Manuf. 31 (2020) 100909.

[56] F. Wirth, Process Understanding, Modeling and Predictive Simulation of Laser Cladding (Ph.D. thesis), ETH Zurich, 2018.
[57] P. Zhang, X. Zhou, X. Cheng, H. Sun, H. Ma, Y. Li, Elucidation of bubble evolution and defect formation in directed energy deposition based on direct observation, Addit. Manuf. 32 (2020) 101026.
[58] C. Cagran, Thermal Conductivity and Thermal Diffusivity of Liquid Copper (Ph.D. thesis), Technische Universitat Graz, 2000.
[59] J. Schmitz, J. Brillo, I. Egry, R. Schmid-Fetzer, Surface tension of liquid Al–Cu binary alloys, Int. J. Mater. Res. 100 (11) (2009) 1529–1535.
[60] A. Dinsdale, P. Quested, The viscosity of aluminium and its alloys–A review of data and models, J. Mater. Sci. 39 (2004) 7221–7228.
[61] M. Leitner, T. Leitner, A. Schmon, K. Aziz, G. Pottlacher, Thermophysical properties of liquid aluminum, Met. Mater. Trans. A 48 (2017) 3036–3045.
[62] A. Kurochkin, P.S. Popel', D.A. Yagodin, A. Borisenko, A. Okhapkin, Density of copper-aluminum alloys at temperatures up to 1400°c determined by the gamma-ray technique, High Temp. 51 (2) (2013) 197–205.
[63] J.B. Edwards, E. Hucke, J. Martin, Diffusion in binary liquid-metal systems, Metall. Rev. 13 (1) (1968) 1–28.
[64] N. Isono, P.M. Smith, D. Turnbull, M. Aziz, Anomalous diffusion of Fe in liquid Al measured by the pulsed laser technique, Met. Mater. Trans. A 27 (1996) 725–730.
[65] J.M. Quaresma, C.A. Santos, A. Garcia, Correlation between unsteady-state solidification conditions, dendrite spacings, and mechanical properties of Al-Cu alloys, Met. Mater. Trans. A 31 (2000) 3167–3178.
[66] S. Gill, W. Kurz, Rapidly solidified Al–Cu alloys–II. Calculation of the microstructure selection map, Acta Met. et Mater. 43 (1) (1995) 139–151.
[67] Z. Gu, J. Chen, A probabilistic analysis of some selected mixing indices, Chem. Eng. Res. Des. 93 (2015) 293–303.
[68] J.L. Murray, The aluminium-copper system, Int. Met. Rev. 30 (1) (1985) 211–234.
[69] C.-Y. Chen, W.-S. Hwang, Effect of annealing on the interfacial structure of aluminum-copper joints, Mater. Trans. 48 (7) (2007) 1938–1947.
[70] K. Oh-ishi, K. Edalati, H.S. Kim, K. Hono, Z. Horita, High-pressure torsion for enhanced atomic diffusion and promoting solid-state reactions in the aluminum–copper system, Acta Mater. 61 (9) (2013) 3482–3489.
[71] J.I. Goldstein, D.E. Newbury, J.R. Michael, N.W. Ritchie, J.H.J. Scott, D.C. Joy, Scanning Electron Microscopy and X-Ray Microanalysis, springer, 2017.
[72] M. Zimmermann, M. Carrard, W. Kurz, Rapid solidification of Al-Cu eutectic alloy by laser remelting, Acta Metall. 37 (12) (1989) 3305–3313.
[73] V. Bathula, C. Liu, K. Zweiacker, J. McKeown, J.M. Wiezorek, Interface velocity dependent solute trapping and phase selection during rapid solidification of laser melted hypo-eutectic Al-11at.% Cu alloy, Acta Mater. 195 (2020) 341–357.
[74] Y. Liu, K. Zweiacker, C. Liu, J. McKeown, J. Wiezorek, Transmission electron microscopy of the rapid solidification microstructure evolution and solidification interface velocity determination in hypereutectic Al-20at.% Cu after laser melting, Acta Mater. 263 (2024) 119475.
[75] R. Trivedi, P. Magnin, W. Kurz, Theory of eutectic growth under rapid solidification conditions, Acta Metall. 35 (4) (1987) 971–980.
[76] S. Gill, M. Zimmermann, W. Kurz, Laser resolidification of the Al Al_2Cu eutectic: The coupled zone, Acta Met. et Mater. 40 (11) (1992) 2895–2906.
[77] S. Liu, Y.C. Shin, Additive manufacturing of Ti6Al4V alloy: A review, Mater. Des. 164 (2019) 107552.
[78] J.E. Spinelli, D.M. Rosa, I.L. Ferreira, A. Garcia, Influence of melt convection on dendritic spacings of downward unsteady-state directionally solidified Al–Cu alloys, Mater. Sci. Eng.: A 383 (2) (2004) 271–282.
[79] E. Sullivan, J. Tomko, J. Skelton, J. Fitz-Gerald, P. Hopkins, J. Floro, Lamellar instabilities during scanning laser melting of Al–Cu eutectic and hypoeutectic thin films, J. Alloys Compd. 865 (2021) 158800.
[80] S. Gaudez, M. Ben Haj Slama, E. Héripré, L. Yedra, M. Scheel, S. Hallais, M. Upadhyay, A synchrotron transmission X-ray microscopy study on precipitate evolution during solid-state thermal cycling of a stainless steel, Addit. Manuf. 73 (2023) 103692.
[81] Y. Bai, C. Zhao, Y. Zhang, J. Chen, H. Wang, Additively manufactured CuCrZr alloy: Microstructure, mechanical properties and machinability, Mater. Sci. Eng.: A 819 (2021) 141528.
[82] Q. Lei, B.P. Ramakrishnan, S. Wang, Y. Wang, J. Mazumder, A. Misra, Structural refinement and nanomechanical response of laser remelted Al-Al_2Cu lamellar eutectic, Mater. Sci. Eng.: A 706 (2017) 115–125.
[83] A. Elmustafa, D. Stone, Indentation size effect in polycrystalline F.C.C. metals, Acta Mater. 50 (14) (2002) 3641–3650.
[84] K.C. Mills, Y.C. Su, Review of surface tension data for metallic elements and alloys: Part 1 – pure metals, Int. Mater. Rev. 51 (6) (2006) 329–351.
[85] Y. Zhang, S. Wu, Z. Guo, G. Peng, L. Wang, W. Yan, Defects caused by powder spattering and entrainment in laser powder bed fusion process: High-fidelity modeling of gas, melt pool and powder dynamics, Acta Mater. 288 (2025) 120816.
[86] M. Vermot des Roches, A.E. Gheribi, P. Chartrand, A versatile multicomponent database for the surface tension of liquid metals, Calphad 65 (2019) 326–339.
[87] A. Özsoy, W.A. Hearn, S. Gaudez, R. Jeswani, Y. Chen, A. Rack, Z. Hegedüs, N. Casati, R.E. Logé, S. Van Petegem, Deconvoluting cracking mechanisms in fusion processing of steel-copper multi-materials via operando X-ray characterisation, Virtual Phys. Prototyp. 20 (1) (2025) e2526798.
[88] P. Lhuissier, X. Bataillon, C. Maestre, J. Sijobert, E. Cabrol, P. Bertrand, E. Boller, A. Rack, J.-J. Blandin, L. Salvo, et al., In situ 3D X-ray microtomography of laser-based powder-bed fusion (L-PBF)—A feasibility study, Addit. Manuf. 34 (2020) 101271.
[89] M.G. Makowska, F. Verga, S. Pfeiffer, F. Marone, C.S. Chang, K. Florio, C.M. Schlepütz, K. Wegener, T. Graule, S. Van Petegem, Operando tomographic microscopy during laser-based powder bed fusion of alumina, Commun. Mater. 4 (1) (2023) 73.